university of groningen / faculty of science and engineering / biomedical engineering

Automatic segmentation of carotid arteries using Independent Component Analysis for quantitative brain PET

L.A.W. (Laura) Vasbinder
S4487648

Nuclear Medicine & Molecular Imaging Department,
University Medical Centre Groningen

Period: 17/04/2023 - 01/07/2023

A thesis submitted for the bachelor degree of Biomedical Engineering
Bachelor's project BME, WBBE901-15

1st Examiner: Prof. Dr. Ir. C. (Charalampos) Tsoumpas, Nuclear Physicist & Biomedical Engineer at Nuclear Medicine and Molecular Imaging Department, University Medical Centre Groningen

2nd Examiner: Dr. A.T.M. (Antoon) Willemsen, Nuclear Medicine and Molecular Imaging Department, University Medical Centre Groningen

“Continuous improvement is better than delayed perfection”
Mark Twain

Preface

In front of you is the undergraduate thesis "Automatic segmentation of carotid arteries using Independent Component Analysis for quantitative brain PET". This thesis is the final work of my undergraduate studies in Biomedical Engineering (BME) at the University of Groningen. The past two months I have been working with great pleasure and passion on my thesis research which I was allowed to perform at the Department of Nuclear Medicine and Molecular Imaging at the University Medical Center Groningen.

In my younger years, I spent quite a lot of time in hospitals, so the interest in the medical world, and specifically in medical imaging, was piqued at an early age. Partly for this reason, I decided during my bachelor's degree to pursue the specialization of medical imaging. After taking several courses in this specialization, the imaging modality positron emission tomography, or better known as PET, sparked my interest and curiosity even more. Therefore, I was even more pleased to be able to conduct my bachelors research with such an interesting and fascinating topic. It was very interesting to go even deeper into the technology underlying this imaging modality and explore the possibilities of making this modality even more widely applicable with even better patient well-being.

The completion of this research would not have been possible without a number of people who have helped and supported me during this project. First and foremost, I would like to express my gratitude to my (daily) supervisor. I had the opportunity to conduct this research under the daily supervision of Laura Providência, for which I am very grateful. Many thanks for that. I would also like to thank my main supervisor and first examiner Charalampos Tsoumpas, and my second examiner Antoon Willemsen, for reviewing my work and guiding me during the project. My sincere thanks also go to Dr. J. van Sluis and colleagues for providing the data for this study. While conducting this study, I also had help from the Carimas Research team, who selflessly allowed me to use their software. This helped me tremendously during my research and for that I am very grateful. Finally, I would like to express my appreciation to my family and friends, who supported me during the process and who helped me review this thesis.

I like to close with the quote from Mark Twain visible on the previous page: "Continuous improvement is better than delayed perfection". This quote was essential for me while doing my research and writing my thesis. In my opinion, this quote nicely represents the essence of doing research; it is better to continuously improve, than to (want to) do it right the first time.

I hope you enjoy reading this thesis.

Laura Vasbinder

Groningen, July 1, 2023

Abstract

The accurate estimation of a plasma input function is crucial for the quantitative analysis of dynamic PET data. The gold standard to obtain the plasma input function is by arterial blood sampling. The procedure of arterial blood sampling is complex and invasive, and therefore it is of clinical interest to develop a noninvasive alternative to arterial blood sampling. In this study, we investigated the feasibility of obtaining accurate image-derived input functions (IDIF) through automatic segmentation of the carotids using independent component analysis (ICA) and subsequent application of partial volume correction (PVC), as an alternative input function for quantitative brain FDG PET.

Methods: Dynamic FDG PET data of 9 oncology patients was used. The carotids were automatically segmented using the FastICA algorithm, and the resulting time activity curves (TAC) were corrected for the partial volume effect (PVE). The corrected TACs were then used as input functions for kinetic modeling using a two-tissue compartment irreversible tracer model and Patlak analysis. The obtained model parameters were compared to reference values that were obtained by kinetic modeling with a reference IDIF extracted from the ascending aorta.

Results: The shape and temporal characteristics of the PVE-corrected carotids TACs resembled those of the reference, indicating reliable estimation. The results obtained by kinetic modeling showed a good agreement between the estimated values for the net influx rate estimated by the PVE-corrected carotids TAC and the reference TAC. The PVE correction effectively minimized the PVE, resulting in improved accuracy of the estimated model parameters.

Conclusion: The obtained results suggest that an IDIF obtained from automatic segmentation of the carotids by ICA and corrected for the PVE can accurately be used as an alternative input function for Patlak analysis. The variation in the estimates of the model parameters K_1, k_2, and k_3 obtained by compartment modeling suggests that the PVE-corrected carotids IDIF cannot be used as an accurate alternative input function for compartment modeling.

Keywords: Carotids time activity curve, compartment modeling, image-derived input function, independent component analysis, partial volume correction, Patlak analysis, quantitative PET.

Contents

Glossary

C_{AA} = time activity curve extracted from the ascending aorta

C_{IC} = time activity curve extracted from the carotids

$C_{IC\text{-}PVC}$ = partial volume corrected time activity curve of the carotids

C_{Tissue} = time activity curve of the tissue surrounding the carotids

C_{True} = true time activity curve in the blood pool (carotids)

FDG = 18F-fluorodeoxyglucose

IC = independent component

ICA = independent component analysis

IDIF = image-derived input function

LC = Lumped Constant

MPE = mean percentage error

MR_{Glu} = cerebral metabolic rate of glucose

PET = positron emission tomography

PG = concentration of glucose in the plasma

PKIN = PMOD Kinetic Modeling

PVC = partial volume correction

PVE = partial volume effect

RC = recovery coefficient

SP = spill-in coefficient

SUV = standardized uptake value

TAC = time activity curve

VOI = volume of interest

2TC3K_VB = two-tissue compartment irreversible tracer model fitting for blood volume

Introduction

Quantitative brain positron emission tomography (PET) studies can be performed to measure several physiological processes, such as volume of distribution, glucose consumption, and cerebral blood flow [Tai and Piccini, 2004]. A radioactive tracer that is often used for quantitative brain PET studies is 18F-fluorodeoxyglucose (FDG), a glucose analog labeled with fluorine-18 [Bell and Deng, 2019]. Semi-quantitative methods, such as the calculation of the standardized uptake value (SUV) for a specific tissue, can provide information about the uptake of FDG into the tissue [Thie, 2004]. The SUV is a measure of the total tracer uptake in the tissue and is proportional to the tissue radioactivity concentration measured in a specific region of interest of a static PET image. However, this total uptake of radioactive tracer is due to three processes: the non-specific accumulation of the radioactive tracer in the tissue by, for example, passive diffusion, the specific interaction of the radioactive tracer with the process of interest (the rate of glucose metabolism in the case of FDG brain PET studies), and the presence of radioactive tracer in the blood vessels that vascularized the tissue [Weber, 2010]. When the aim of the study is to assess the glucose metabolic rate, a fully quantitative analysis must be used to extract the specific FDG uptake from the total uptake measured in the tissue of interest.

Fully quantitative analysis of the dynamic PET data of the brain is done by applying a pharmacokinetic model to the brain time activity curves (TAC). Local cerebral glucose metabolism in parts of the brain can be quantified by the use of a two-tissue compartment irreversible tracer model [Rahmim *et al.*, 2018]. Since the distribution and metabolism of a radioactive tracer is a dynamic process, the plasma tracer radioactivity concentration must be measured and used as an input function to establish and solve compartment models [Heurling *et al.*, 2017]. The input function represents the continuous radioactivity concentration in the plasma over time [Watabe *et al.*, 2006] and is traditionally obtained via arterial blood sampling [Meikle *et al.*, 2021]. Since arterial blood sampling is an invasive and complex procedure that comes with risks to both patients and personnel, there would be much to gain from an alternative method that minimizes or eliminates the need for arterial blood sampling.

In previous years, many non- or less invasive alternatives to obtain the input function have been explored [Mejia *et al.*, 1994; van der Weijden *et al.*, 2023; Zanotti-Fregonara, Chen, *et al.*, 2011]. A popular alternative is the use of an image-derived input function (IDIF) in which the plasma time activity curve is obtained by the placement of a volume of interest (VOI) over a blood pool that is within the field-of-view of the PET scanner [Zanotti-Fregonara, Maroy, *et al.*, 2009]. This approach avoids the need for blood sampling to obtain the input function. However, since there are still quite some challenges to be solved for IDIF, it is still virtually not used in the clinic to reduce the invasiveness of brain PET studies [Zanotti-Fregonara, Chen, *et al.*, 2011]. One challenge often encountered in PET imaging, and also in the IDIF approach, is the partial volume effect (PVE), which becomes relevant when the object size is less than two to three times the PET spatial resolution (3-6 mm). When the IDIF is extracted from large blood pools such as the left ventricle or the aortic segments, PVE can usually be neglected, given the large size of these structures. However, when using a PET scanner with a standard field-of-view (15-25 cm) for dynamic brain PET imaging, these large structures are not in the field-of-view of the PET scanner, and therefore the (internal) carotids are commonly used to extract the IDIF. The internal carotid is a small artery, typically with a diameter of 4.66 ± 0.78 mm for women and 5.11 ± 0.87 mm for men [Krejza *et al.*, 2006], in the neck that supplies blood to the anterior part of the brain. The internal carotid is a branch of the common carotid artery, which splits into the internal and external carotid at the level of the fourth cervical vertebra [Charlick and Das, 2022]. Because of the small size of the internal carotids compared to the typical spatial resolution of a PET scanner [Wang, 2018], they will suffer from PVEs, which can lead to biased model parameters. In 1998, Chen *et al.* proposed a method to correct for the PVE encountered in small anatomical structures.

The aim of this study is to obtain accurate image-derived input functions through automatic segmentation of the carotids by independent component analysis (ICA) and applying the partial volume correction (PVC) method proposed by Chen *et al.* (1998). The time activity curves that were corrected for the PVE were then used for tracer kinetic modeling using a two-tissue compartment irreversible tracer model and Patlak Analysis, and were compared to reference values obtained from kinetic modeling with an IDIF extracted from the ascending aorta.

Theoretical background

Independent Component Analysis

Independent Component Analysis (ICA) is a statistical tool that uses computational analysis to identify and separate the original signals coming from individual sources in a signal that is a linear combination of these sources [Dieckmann, 2023]. One key assumption for the use of ICA is that the individual sources are statistically independent [Hyvärinen and Oja, 2000]. The measured, mixed signal can then be defined as

$$x_i \ = \ a_{i,1} \ * \ s_1 \ + a_{i,2} \ * \ s_2 \ + \ ... + \ a_{i,n} \ * \ s_n \ = \sum_n \ a_{i,n} \ * \ s_n \tag{1}$$

Where x_i is the i^{th} measured mixed signal, s_n is the n^{th} independent source signal, and $a_{i,n}$ is the corresponding unknown mixing coefficient. The above function can be represented using matrix notation as follows

$$\mathbf{x} = \mathbf{As} \tag{2}$$

Where $\mathbf{x}$ is the space that contains all i measured mixed signals, the n independent source signals, or independent components (ICs), are represented by the random vector $\mathbf{s}$, and matrix $\mathbf{A}$ contains the corresponding mixing coefficients [Tharwat, 2020]. The ultimate goal of ICA is to solve Equation 2 for the vector $\mathbf{s}$ by finding the matrix $\mathbf{A}$ or the matrix $\mathbf{W}$, which is the inverse of matrix $\mathbf{A}$, for which the sources have the maximum possible independence. A way to maximize the independence of sources is by maximizing their non-Gaussianity. The second fundamental theorem of probability, also called the Central Limit Theorem, states that, under certain conditions, the distribution of a sum of independent variables will follow a Gaussian distribution [Grinstead and Snell, 2022]. And, in general, a signal which is a mixture of independent random variables has a more Gaussian distribution than any of the individual variables. Maximizing the non-Gaussianity will therefore result in the recovery of the independent variables hidden in the mixed signal [Cardoso, 2003].

One way to measure non-Gaussianity is by measuring the negative entropy, often called negentropy. The negentropy is zero in the case where all the variables are Gaussian and maximal in the case where all variables are maximal independent [Kumar and Jayanthi, 2019]. For this study, the FastICA algorithm was used. This algorithm maximizes the negentropy for the independent source signals by the use of fixed-point iterations [Hyvarinen, 1999] and thereby extracts the independent components.

Partial volume correction

The partial volume effect (PVE) causes the radioactivity concentration of small, highly active targets to be underestimated while overestimating their apparent volume due to spill-out from the target area into the background. On the other hand, larger structures or regions with lower tracer uptake may appear smaller or have higher measured tracer concentrations due to spill-in from the background into the target tissue [Bettinardi *et al.*, 2014]. The effect of spill-in and spill-out taken together is referred to as the spill-over of radioactivity. In order to obtain an accurate carotids TAC, the curve should be corrected for the PVE. A method to correct the obtained TAC for spill-out and spill-in was proposed by Chen *et al.* (1998). In this method, it is assumed that the radioactivity measured in the carotids is actually a linear combination of the true radioactivity in the blood pool and the radioactivity present in the tissue surrounding the carotids. Consequently, the measured radioactivity in the carotids can be represented as:

$$C_{\text{IC}} = \ C_{\text{True}} \ * \ RC \ + \ C_{\text{Tissue}} \ * \ SP \tag{3}$$

where C_{IC} is the obtained carotids TAC, C_{True} is the true tracer concentration in the blood pool, C_{Tissue} is the tracer concentration in the tissue surrounding the carotids, RC is the recovery coefficient and SP is the spill-over coefficient representing the spill-over of activity between the surrounding tissue and the carotids. One can then estimate the values for RC and SP by applying Equation 3 for the time-points for which the C_{IC} , C_{True}, and C_{Tissue} are known and subsequently applying the non-negative linear least squares method.

Materials and methods

Data acquisition

For this study, dynamic FDG PET data of 9 oncology patients (5 male, 4 female; age range: 68–81 years, mean age: 73.1 ± 3.9) with suspected lung malignancy referred for clinical diagnosis, who participated in a previous study [van Sluis *et al.*, 2022] was used. Listmode PET data were acquired on a Siemens Biograph Vision Quadra for 65 minutes after intravenous bolus injection of 3 MBq/kg (±10%) [18F]FDG (activity range: 204-303 MBq, mean activity: 246.0 ± 33.6 MBq). Patients were asked to fast at least 6 hours prior to the PET scan. The data was binned over 42 frames (four frames of 10 s, sixteen of 5 s, six of 30 s, five of 60 s, and eleven frames of 300 s), and the images were reconstructed using a 3D OSEM PSF-TOF algorithm (4 iterations, 5 subsets). All data was corrected for attenuation, random coincidences, scattered radiation, dead-time, and decay. The reconstructed images consisted of 645 planes of 440x440 voxels, with a voxel size of 1.65 × 1.65 × 1.65 mm^3. No filter was applied to the images.

Inter-frame motion correction was performed on the slices comprising the head and neck using a cubic spline interpolation. The correction was applied when translational motion in any of the directions (x, y, or z) was higher than 3 mm.

For most parts of this study, only the portion of the obtained dynamic FDG PET data that contains the head and neck region (planes 500 to 645) was used. This portion of the total data will be referred to as "dynamic brain FDG PET data". The portion of the obtained dynamic FDG PET data that contains the chest region (planes 350 to 500) was used for the Partial Volume Correction and validation, and will be referred to as "dynamic chest FDG PET data".

Determination of the carotid volume of interest

To ensure that only the carotid structures will be segmented, the original dynamic brain FDG PET data was cropped before applying ICA to select only the volume in which the carotid structures were clearly visible. To define this volume, the first five image frames of the dynamic brain FDG PET data (first 50 seconds) were summed to easily identify the carotids. A cubical VOI of size 110x180x65 voxels was then defined that encloses both the left and right carotid arteries and the data was cropped to this VOI.

FastICA for dynamic brain FDG PET data

Dynamic brain FDG PET data are four-dimensional datasets that contain information about the measured radioactivity (kBq/cc) in each voxel of the image. The measured radioactivity signal as a function of the location in the image can be treated as a mixed signal $\mathbf{x}(q)$, where q represents the voxel number. The elements of $\mathbf{x}(q)$, $x_i(q)$, represent the measured signal in voxel q at time-point i. The time-point i is the time-point at which the signal is measured. As described before, for this study 42 frames were acquired with different frame times. Therefore, the time-point i ranged from 1 to 42. The independent components were represented by $\mathbf{s}(q)$, which represents the voxels in the independent components. This matrix containing the source information provides information about the spatial location of the independent components and thus the spatial distribution of the tissues of interest, corresponding to the independent components. The independent source matrix of size n x q was then split into n matrices of size 1 x q representing the information for the n individual independent components. These matrices were reshaped to the x, y, and z dimensions of the original dynamic brain FDG PET data and visualized as independent component images.

For this study, it was assumed that the dynamic brain FDG PET data is composed of two individual sources, or independent components, namely blood and other tissue. Therefore, the ICA algorithm was used to separate the original PET image into a blood- and tissue-independent component image. The blood-independent component image represents the blood pool in the dynamic brain FDG PET data which, in this case, are the carotid arteries.

Pre-processing

Before applying the FastICA algorithm to the dynamic brain FDG PET data, pre-processing of the data was done. As previously mentioned, the dynamic brain FDG PET data was represented as the matrix $\mathbf{x}$. The data pre-processing phase consisted of two parts, centering and whitening of $\mathbf{x}$ [Tharwat, 2020]. In the first step, it is necessary to transform $\mathbf{x}$ into a variable with a zero mean. This centering of $\mathbf{x}$ was done by subtracting its mean. The second part, whitening of $\mathbf{x}$, was done to un-correlate its components and make their variances equal to one.

Obtaining the carotids time activity curve

To obtain the TAC of the carotid arteries, a vessel mask was created from the blood-independent component image. By definition of the theorem underlying the ICA algorithm, the distribution of the data in the independent component images is assumed to be super-Gaussian [Hyvarinen, 1999; Hyvärinen and Oja, 2000]. Therefore, the method of Gaussian fitting proposed by Su *et al.* (2005) was used to determine the threshold for obtaining the vessel mask. First, a histogram was plotted of the number of voxels in the image having a specific gray value. This histogram was then transformed using the Gaussian fitting method, by subtracting the mean of the histogram values from these histogram values and dividing it by its standard deviation, as shown in Equation 4. After transformation, the desired threshold value was determined from the transformed histogram and was used to create the vessel mask. For this study, the threshold was set to 9 times the standard deviation. Finally, the carotids TAC ($\mathrm{C_{IC}}$) was obtained by applying the generated vessel mask to the dynamic brain FDG PET data and averaging the TACs of the voxels inside the mask.

$$Z = \frac{X - \mu}{\sigma} \tag{4}$$

Partial Volume Correction

The previously obtained $\mathrm{C_{IC}}$ can be represented as the linear combination in Equation 3. To obtain the TAC of the surrounding tissue ($\mathrm{C_{Tissue}}$), the previously created vessel mask was dilated using both a 3×3×3 and 5×5×5 structuring element. The mask of the tissue surrounding the carotid arteries was then acquired by subtracting the smaller mask (3×3×3 dilation) from the larger mask (5×5×5 dilation). The radioactivity of the surrounding tissue was obtained by applying the resultant mask to the dynamic brain FDG PET data and averaging the TACs of the voxels inside the mask.

C_{True} was substituted by $\mathrm{C_{AA}}$ and represents the true radioactivity in the blood pool obtained by extracting an IDIF from the ascending aorta. The TAC was generated by placing a spherical VOI with a radius of 7.5 mm in the middle of the ascending aorta structure in the dynamic chest FDG PET data and averaging the TACs of the voxels inside the VOI. To determine the right location of the VOI, the ascending aorta structure was first identified by visually inspecting an early image frame where the contrast between the blood pool and the surrounding tissues was high. For the PVC, the measurements of the last three time frames of the ascending aorta TAC were used.

Equation 3, representing the linear mixture of measured radioactivity in the carotids, was applied to the three time-points for which $\mathrm{C_{IC}}$, $\mathrm{C_{Tissue}}$, and $\mathrm{C_{AA}}$ were all known, i.e. the last three frames (50 - 65 min). The non-negative linear least squares method was then used to estimate the values of the recovery and spill-over coefficients; the coefficients were bound to have a value between zero and one. After estimating the coefficients, the PVE-corrected carotids TAC, $\mathrm{C_{IC\text{-}PVC}}$, was calculated as:

$$C_{IC-PVC} = \frac{C_{IC} - SP * C_{Tissue}}{RC} \tag{5}$$

Two-tissue compartment modeling

Quantitative analysis of the dynamic brain FDG PET data was done by performing compartment modeling and Patlak analysis. The tracer kinetics of FDG can be represented using a two-tissue compartment model [Huang *et al.*, 1980; Vallabhajosula, 2023] as shown in Figure 1.

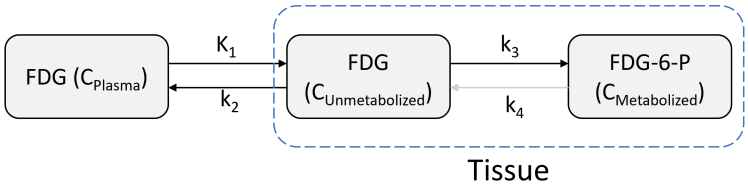

Figure 1: Schematic representation of the two-tissue compartment model for modeling the kinetics of FDG. The model represents the three possible tracer states, FDG in plasma, FDG in brain tissue, and phosphorylated FDG in tissue. The parameters K_1 to k_4 represent the rate constants between the compartments.

The model consists of three compartments, a compartment representing the FDG concentration in plasma, a compartment representing the FDG concentration in the brain tissue, and a compartment representing the concentration of phosphorylated FDG, FDG-6-P, in the brain tissue. These three compartments are represented by C_{Plasma}, $C_{Unmetabolized}$, and $C_{Metabolized}$, respectively. The model parameters K_1, k_2, k_3, and k_4 represent the influx of FDG from the plasma to the tissue, the efflux of FDG from the tissue to the plasma, the rate of FDG phosphorylation, and the rate of FDG dephosphorylation, respectively. Although dephosphorylation of FDG is possible to some extent, this process in brain tissue is very slow [Kilicoglu *et al.*, 2023] and has shown to have no significant effect in the time span of the PET data acquisition [Schmidt *et al.*, 1992]. Therefore, the rate constant k_4 was set to zero and a two-tissue compartment irreversible tracer model fitting for blood volume (2TC3K_VB) was used to estimate the model parameters K_1, k_2, and k_3.

The model parameters were estimated using the PMOD Kinetic Modeling (PKIN) tool [https://doc.pmod.com/PDF/PKIN.pdf]. A plasma input curve and a tissue TAC representing the concentration of FDG in the whole brain were provided to the software to initiate the fitting. The whole-brain TAC was obtained by applying a mask of the whole brain to the dynamic brain FDG PET data and averaging the TACs for all voxels in the brain mask. Before fitting the model, blood delay correction was applied to correct for the time delay between the blood and tissue TACs.

The analyses for all patients were performed threefold, using the same tissue TAC but different plasma input functions. First, the analyses were performed using C_{IC} as a plasma input function. Then, using $C_{IC\text{-}PVC}$. Lastly, the analyses were performed with C_{AA} as the input function, which is used as a reference for this study. The rate constants were then used to compute the net influx rate of FDG by

$$K_i = \frac{K_1 * k_3}{k_2 + k_3} \tag{6}$$

The parameter K_i is a measure of the concentration of FDG that is trapped in the irreversible phosphorylated state and can be used to calculate the cerebral metabolic rate of glucose (MR_{Glu}) by [Huang *et al.*, 1980]

$$MR_{Glu} = \frac{PG}{LC} * K_i \tag{7}$$

where PG is the concentration of glucose in the plasma and LC is the Lumped Constant.

Patlak analysis

Another method that was used to obtain the regional, whole-brain net influx rate of FDG was the graphical Patlak analysis. The Patlak analysis is a graphical analysis technique that can be used for tracers that undergo irreversible trapping in tissue. For the Patlak analysis, the measured tissue TAC is mathematically transformed and plotted as a function of normalized time [Jodal, 2004], known as the Patlak plot, which results in a straight line when the reversible compartment is in equilibrium with plasma. For this study, the time of equilibrium was set to $t^* = 30$ min. The slope of the Patlak plot is equal to the net influx rate K_i and the intercept is equal to the sum of the distribution volume of the reversible compartment and the fractional blood volume.

After regional quantitative analysis, voxel-by-voxel analysis was done by creating parametric images of the net influx rate K_i with both the PVE-corrected IDIF and the ascending aorta IDIF as input functions. The Patlak analysis method was used to create the parametric images. To generate the parametric net influx rate images, the same whole-brain mask was used as for the regional, whole-brain analysis. Whereas an average of all TACs for the different voxels inside the mask was taken for the regional analysis, all voxel TACs were used individually to generate the parametric images.

Data analysis

For this study, the model parameters obtained by using C_{AA} as the input function were used as the reference. The first step of the data analysis was visual analysis to qualitatively determine if there was variation between the three input functions and their corresponding estimated model parameters. After the visual analysis, the area under the curve (AUC) for all C_{IC}, $C_{IC\text{-}PVC}$, and C_{AA} was determined.

To quantitatively assess whether performing the partial volume correction improved the estimation of the model parameters, the mean percent error (MPE) of the obtained parameters was determined for the comparison of C_{IC} vs C_{AA} and for the comparison of $C_{IC\text{-}PVC}$ vs C_{AA}. The MPE is defined as

$$MPE = \frac{100\%}{n} * \sum_{n} \frac{estimate - actual}{actual} \tag{8}$$

The Wilcoxon signed-rank test with a significance level of 0.05 was performed to test the hypothesis of zero mean difference between the model parameters estimated using either C_{IC} or $C_{IC\text{-}PVC}$ as input function, and the parameters estimated by taking C_{AA} as input function.

For both the regional and voxel-wise analysis, the net influx rates obtained with both C_{IC} and $C_{IC\text{-}PVC}$ as input were compared to the net influx rates estimated using C_{AA} by creating a regression plot and performing regression analysis. When the values obtained with the two input functions are in perfect agreement, the slope of the regression line and the coefficient of determination would be exactly one, and the intercept would be zero. Obtained measures close to these values thus imply a good agreement between the two methods. The Wilcoxon signed-rank test was used to test the unit slope and zero intercept, with a significance level of 0.05.

In addition, a Bland-Altman plot was generated for each patient to see whether there was systemic and/or proportional bias in the estimated voxel-wise net influx rates by $C_{IC\text{-}PVC}$ and C_{AA}. To investigate systemic bias, the mean difference lines in the Bland-Altman plots for all patients were examined. If this line was significantly different from zero, it indicates the presence of systemic bias. The Wilcoxon signed-rank test was performed to determine whether the observed mean differences were significantly different from zero. To examine proportional bias, the linearity of the differences was assessed for each plot. This was done by plotting a regression line on the Bland-Altman plot; if the regression line has a significant slope, this indicates a proportional bias. The Wilcoxon signed-rank test was again consulted to assess whether there was a significant slope.

Results

Regional analysis

Figure 2A shows the contours of the carotids vessel mask obtained by ICA and Gaussian fitting (red) and the tissue mask obtained by the dilation method (blue) for one of the patients. The masks are superimposed over an early frame of one brain level where the carotid structure was easily seen. Figure 2B shows the TACs for C_{IC} and C_{Tissue}, obtained by applying the masks from Figure 2A to the dynamic brain FDG PET data. The original and PVE-corrected IDIFs extracted from the carotids were compared to the IDIF extracted from the ascending aorta. Figure 3 shows the TACs C_{IC}, $C_{IC\text{-}PVC}$, and C_{AA}, for two different patients. C_{IC} and $C_{IC\text{-}PVC}$ are the carotids TAC before and after partial volume correction, respectively, and C_{AA} is the TAC extracted from the ascending aorta. It can be seen that for the patient in Figure 3A, the peak of $C_{IC\text{-}PVC}$ is higher than the peak of C_{AA}. For the patient in Figure 3B, the opposite is true. For both patients, the tails of $C_{IC\text{-}PVC}$ and C_{AA} coincided well. The mean C_{IC}, $C_{IC\text{-}PVC}$, and C_{AA} for the nine patients are shown in Figure 4. From Figure 4 it can be seen that, on average, the peak of C_{IC} is significantly lower than the peaks of $C_{IC\text{-}PVC}$ and C_{AA}. The peak of the mean C_{IC} was 46% lower than that of C_{AA} and the peak of the mean $C_{IC\text{-}PVC}$ was found to be 11% lower than the peak of C_{AA}. Furthermore, it can be seen that all three curves reach their peak at the same time-point and have similar temporal characteristics. In the latter parts of the graph, the curve of C_{IC} underestimates C_{AA} by 17% in the last frame and the lines of $C_{IC\text{-}PVC}$ and C_{AA} lie on top of each other and are almost equal (difference of 0.40% in the last frame). Furthermore, the AUC for the mean C_{IC}, $C_{IC\text{-}PVC}$, and C_{AA} in Figure 4 were 450, 627, and 651 min x kBq x cc^{-1}, respectively.

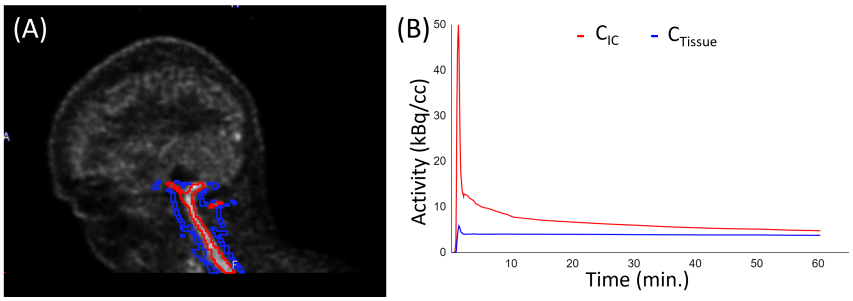

Figure 2: **(A)** Example of the contours of the obtained carotids vessel mask (red) and tissue mask (blue) for one of the patients. The carotids vessel mask was obtained by independent component analysis and Gaussian fitting. The tissue mask was obtained by dilation and subtraction of the carotids vessel mask. **(B)** Time activity curves obtained by applying the masks of (A) to the dynamic brain FDG PET data.

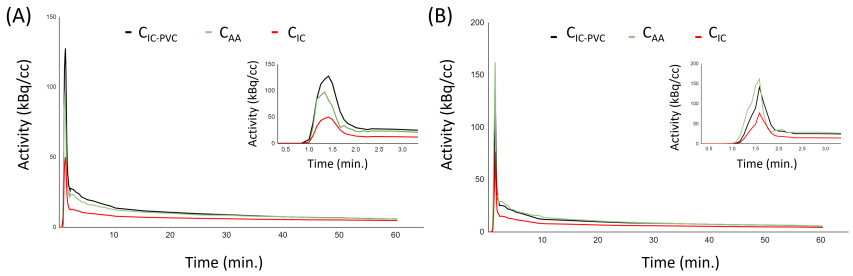

Figure 3: For two patients, the original and partial volume corrected carotids time activity curves (C_{IC} and $C_{IC\text{-}PVC}$, respectively) and the reference time activity curve extracted from the ascending aorta (C_{AA}). The partial volume corrected TAC $C_{IC\text{-}PVC}$ for the patient in **(A)** has a higher peak than the TAC C_{AA} has. Opposite to what can be seen in (A), for the patient in **(B)** the peak of $C_{IC\text{-}PVC}$ is lower than the peak of C_{AA}. For both patients, the tails of $C_{IC\text{-}PVC}$ and C_{AA} coincided well.

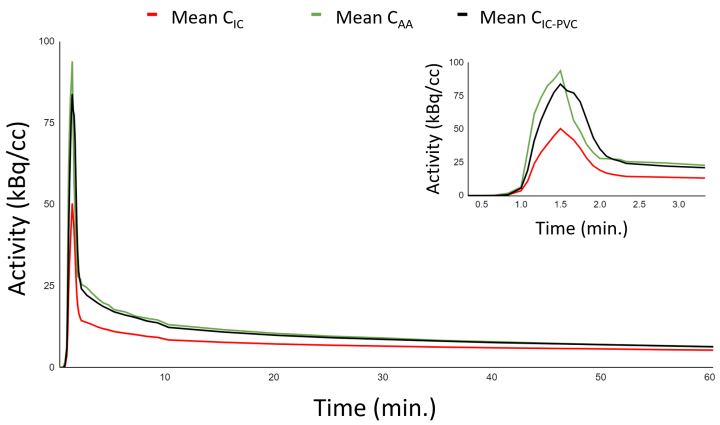

Figure 4: Comparison of the mean original and PVE-corrected carotids time activity curves (Mean C_{IC} and Mean $C_{IC\text{-}PVC}$, respectively), and the mean time activity curve extracted from the ascending aorta (Mean C_{AA}). The time activity curves are acquired by taking the mean of the time activity curves of all nine patients. On average, the peak of C_{IC} is significantly lower than the peaks of $C_{IC\text{-}PVC}$ and C_{AA}. All three curves show similar temporal characteristics.

To assess if the results of the analyses using the carotids IDIFs are accurate and could potentially be used as an alternative to kinetic modeling with arterial blood sampled input curves, the observed values for the model parameters estimated with both C_{IC} and $C_{IC\text{-}PVC}$ were compared to the observed values estimated using C_{AA} as the input function. The first step of the comparison was the visual analysis of the results using bar charts, as can be seen in Figures 5A-5E. These charts show the estimated values for the model parameters with the three different input functions, for all nine patients. The mean and standard deviation of the values obtained for the parameters K_1, k_2, k_3, K_i for irreversible two-tissue compartment modeling, and K_i for Patlak analysis, with C_{IC}, $C_{IC\text{-}PVC}$, and C_{AA} as subsequent input functions are shown in Table 1.

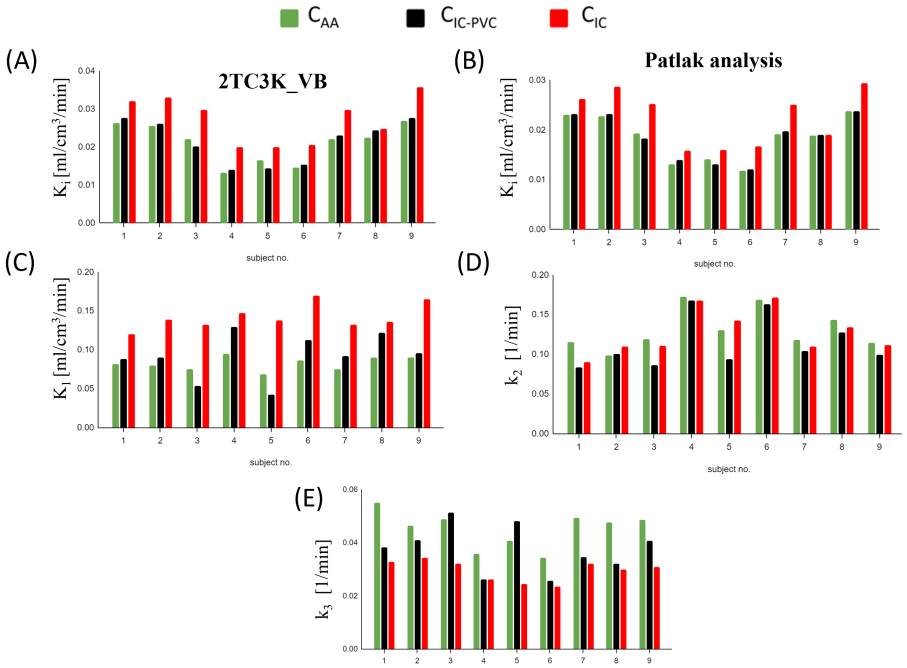

Figure 5: Comparison of the model parameters obtained with the C_{IC} and $C_{IC\text{-}PVC}$ to the results obtained with C_{AA}. Comparison of the values obtained with all three input functions for **(A)** the net influx rate obtained with irreversible two-tissue compartment modeling, **(B)** the net influx rate obtained with Patlak analysis **(C)** K_1, **(D)** k_2, and **(E)** k_3.

Table 1: Comparison of the mean model parameters estimated by the use of the two-tissue compartment irreversible model (2TC3K_VB) and Patlak analysis and C_{IC}, $C_{IC\text{-}PVC}$, and C_{AA} as subsequent input functions. The model parameters estimated by C_{IC} and $C_{IC\text{-}PVC}$ are compared to the model parameters estimated by C_{AA} using the Wilcoxon signed-rank test and the mean percentage errors (MPE). The p-values for the Wilcoxon signed-rank tests are shown in columns 4 and 8.

	C_{IC}	**C_{AA}**	**p-value**	**MPE**	**$C_{IC\text{-}PVC}$**	**C_{AA}**	**p-value**	**MPE**
2TC3K_VB								
K_1 [ml/cm^3/min]	0.14 ±0.02	0.083 ±0.009	0.03	73 ±19%	0.09 ±0.03	0.083 ±0.009	0.2	9.3 ±27%
k_2 [1/min]	0.13 ±0.03	0.13 ±0.03	0.5	-2.9 ±9.9%	0.11 ±0.03	0.13 ±0.03	0.03	-14 ±11%
k_3 [1/min]	0.030 ±0.004	0.045 ±0.007	0.03	-34 ±5.2%	0.038 ±0.009	0.045 ±0.007	0.06	-17 ±18%
K_i [ml/cm^3/min]	0.027 ±0.006	0.021 ±0.005	0.03	31 ±12%	0.021 ±0.006	0.021 ±0.005	0.5	1.5 ±7.3%
Patlak analysis								
K_i [ml/cm^3/min]	0.023 ±0.006	0.019 ±0.004	0.03	23 ±12%	0.019 ±0.005	0.019 ±0.004	0.5	0.24 ±4.3%

To quantitatively compare the results obtained with the C_{IC} and $C_{IC\text{-}PVC}$ to the reference values, the mean percent error (MPE) of the model parameters for both C_{IC} vs C_{AA} and $C_{IC\text{-}PVC}$ vs C_{AA} was calculated (fifth and ninth column of Table 1, respectively). Furthermore, the Wilcoxon signed-rank test was performed to test the hypothesis of zero mean difference between the model parameters obtained by C_{IC} and C_{AA}, and the hypothesis of zero mean difference between the parameters obtained by $C_{IC\text{-}PVC}$ and C_{AA} (columns four and eight of Table 1). For the results obtained by compartment modeling, the MPEs of the model parameters K_1, k_2, k_3, and K_i estimated by the C_{IC} vs C_{AA} were found to be 73 ± 19%, -2.9 ± 9.9%, -34 ± 5.2%, and 31 ± 12%, respectively. The MPEs for the parameters estimated by $C_{IC\text{-}PVC}$ compared to C_{AA} were 9.3 ± 27%, -14 ± 11%, -17 ± 18%, and 1.5 ± 7.3%, respectively. For the regional net influx rates obtained with Patlak analysis, the MPE for C_{IC} vs C_{AA} and $C_{IC\text{-}PVC}$ vs C_{AA} were found to be 23 ± 12% and 0.24 ± 4.3%, respectively. The hypothesis of zero mean difference between the model parameters estimated by C_{IC} and C_{AA} was rejected for the model parameters K_1, k_2, K_i obtained from compartment modeling, and K_i obtained with Patlak analysis ($p = 0.03$ for all four parameters). The hypothesis of zero mean difference between the value obtained for the model parameter k_2 by C_{IC} and C_{AA} could not be rejected ($p = 0.5$). For the model parameters K_1, k_3, K_i obtained with compartment modeling, and K_i obtained with Patlak analysis estimated by $C_{IC\text{-}PVC}$ and C_{AA}, the hypothesis of zero mean difference could not be rejected by the Wilcoxon signed-rank test ($p = 0.2$, $p = 0.06$, $p = 0.5$, and $p = 0.5$, respectively). On the other hand, the hypothesis of zero mean difference between the values for the model parameter k_2 estimated by $C_{IC\text{-}PVC}$ and C_{AA} was rejected ($p = 0.03$).

To further analyze the results obtained for the regional net influx rates with all three input functions, regression analysis was performed. The results of the regression analysis are shown in Table 2 and Figure 6. On the y-axes of Figures 6A - 6D, the net influx rates estimated by either C_{IC} or $C_{IC\text{-}PVC}$ are plotted. The x-axes in these figures represent the corresponding net influx rates estimated by C_{AA}. Regression analysis of the results obtained with C_{IC} and C_{AA} for compartment modeling and Patlak analysis gave rise to slopes of 1.1 and 1.2, and intercepts of 3.6×10^{-3} and 1.3×10^{-3}, respectively. The regression analysis for the values obtained by compartment modeling and Patlak analysis with the input functions $C_{IC\text{-}PVC}$ and C_{AA} gave rise to regression slopes and intercepts of 1.1, 1.0, -1.2×10^{-3}, and -6.3×10^{-5}, respectively.

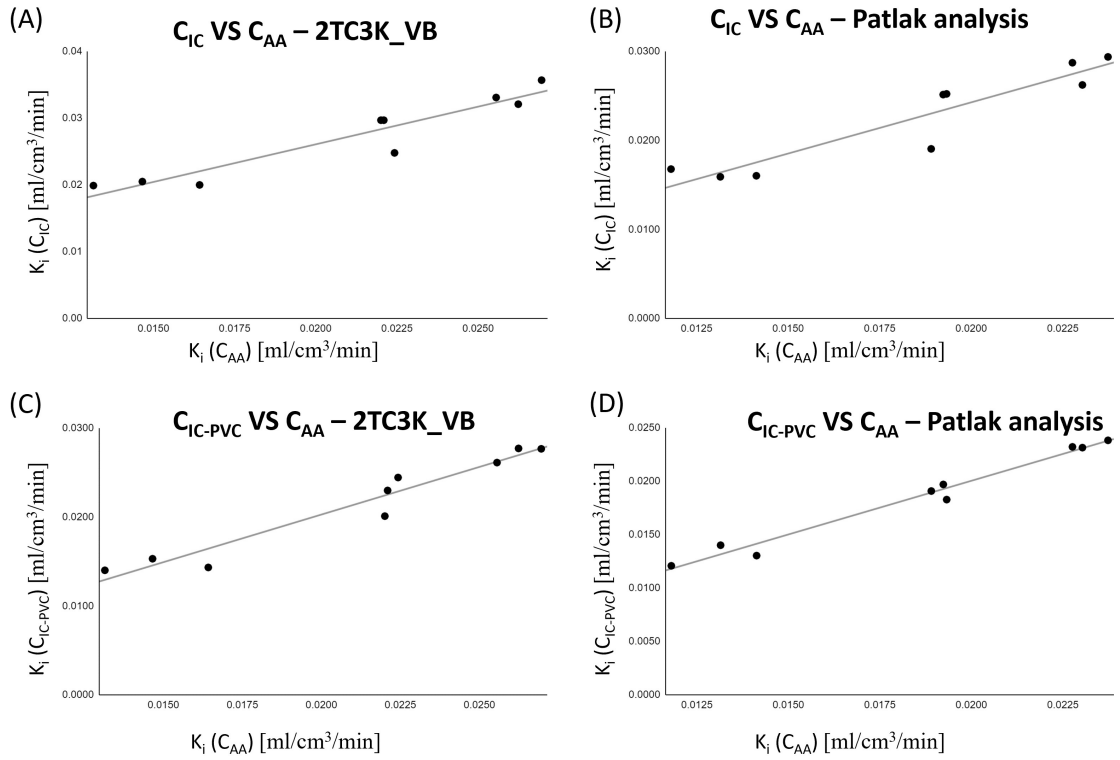

Figure 6: Regression analysis of the regional net influx rates estimated by **(A)** irreversible two-tissue compartment modeling with C_{IC} and C_{AA}, **(B)** Patlak analysis with C_{IC} and C_{AA}, **(C)** irreversible two-tissue compartment modeling with $C_{IC\text{-}PVC}$ and C_{AA}, and **(D)** Patlak analysis with $C_{IC\text{-}PVC}$ and C_{AA}. The y-axes of the figures represent the net influx rates estimated by either C_{IC} ((A) and (B)) or $C_{IC\text{-}PVC}$ ((C) and (D)). The x-axes in these figures represent the corresponding net influx rates estimated by C_{AA}.

Table 2: Summary of the results obtained from regression analyses (shown in Figure 6) of C_{IC} vs C_{AA} and $C_{IC\text{-}PVC}$ vs C_{AA} for the regional net influx rates obtained with irreversible two-tissue compartment modeling (2TC3K_VB) and Patlak analysis. The table shows the results for the regression slope and intercept, and coefficient of determination for all four regression analyses.

	2TC3K_VB		**Patlak analysis**	
	C_{IC} vs C_{AA}	$C_{IC\text{-}PVC}$ vs C_{AA}	C_{IC} vs C_{AA}	$C_{IC\text{-}PVC}$ vs C_{AA}
Slope	1.1	1.1	1.2	1.0
Intercept	3.6×10^{-3}	-1.2×10^{-3}	1.3×10^{-3}	-6.3×10^{-5}
R^2	0.90	0.94	0.87	0.98

Voxel-wise analysis

Subsequently, K_i parametric images were created using the Patlak method. Two sets of K_i parametric images were generated for each patient: one set where $C_{IC\text{-}PVC}$ was used as the input function and the other where C_{AA} was used as the input function. The net influx rate parametric images were used for comparison and were first visually analyzed. Regression analysis was then used to quantitatively compare the voxel-wise net influx rates obtained when using $C_{IC\text{-}PVC}$ and C_{AA} as input functions. Table 3 shows the mean net influx rate for $C_{IC\text{-}PVC}$ and C_{AA}, which were obtained by averaging all voxels in the parametric images, and the results of the regression analysis. The mean regression slope, intercept, and coefficient of determination for the nine patients were 1.03 $\pm$ 0.07, (-6.0 $\pm$ 7.0) x 10^{-4}, and 1.000 $\pm$ 0.003, respectively. Moreover, the mean net influx rate estimated by using $C_{IC\text{-}PVC}$ as the input function was 0.017 $\pm$ 0.004 ml/cm^3/min, whereas the mean net influx rate estimated by using C_{AA} as the input function had a value of 0.018 $\pm$ 0.004 ml/cm^3/min. An example of the voxel-wise regression analysis for one patient is shown in Figure 7. As explained earlier, the regression line would have a slope of one and an intercept of zero when the two methods are in perfect agreement. To test whether this is the case for the net influx rates observed for all nine patients, a Wilcoxon signed-rank test was performed. The test showed that the hypothesis for the unit slope and zero intercept could not be rejected ($p = 0.3$ for the slope and $p = 0.07$ for the intercept). A Bland-Altman plot for the voxel-wise net influx rates for the same patient as in Figure 7 is shown in Figure 8. On the x-axis of Figure 8, the average result, i.e. the average of the net influx rate estimated by $C_{IC\text{-}PVC}$ and C_{AA}, is displayed. The y-axis of Figure 8 represents the difference between the net influx rate estimated by the two input functions, i.e. the net influx rate estimated by $C_{IC\text{-}PVC}$ minus the net influx rate estimated by C_{AA}. The three dashed lines represent, from top to bottom, the upper confidence interval, the mean difference, and the lower confidence interval, respectively. To examine the systemic and proportional bias, the mean differences and regression slopes were assessed. The Wilcoxon signed-rank test showed that there was neither a significant mean difference nor a significant regression slope ($p = 0.95$ for the mean difference and $p = 0.2$ for the slope).

Table 3: Comparison of the voxel-wise net influx rates estimated by $C_{IC\text{-}PVC}$ and C_{AA} by the use of regression analysis. The obtained voxel-wise net influx rates using the two input functions were regressed for each patient individually and the coefficient of determination, and slope and intercept of the regression line were determined. The mean coefficient of determination, and mean slope and intercept of the regression line are shown in the table.

Mean K_i ($C_{IC\text{-}PVC}$) [ml/cm^3/min]	0.017 $\pm$ 0.004
Mean K_i (C_{AA}) [ml/cm^3/min]	0.018 $\pm$ 0.004
Slope	1.03 $\pm$ 0.07
Intercept	(-6.0 $\pm$ 7.0) x 10^{-4}
R^2	1.000 $\pm$ 0.003

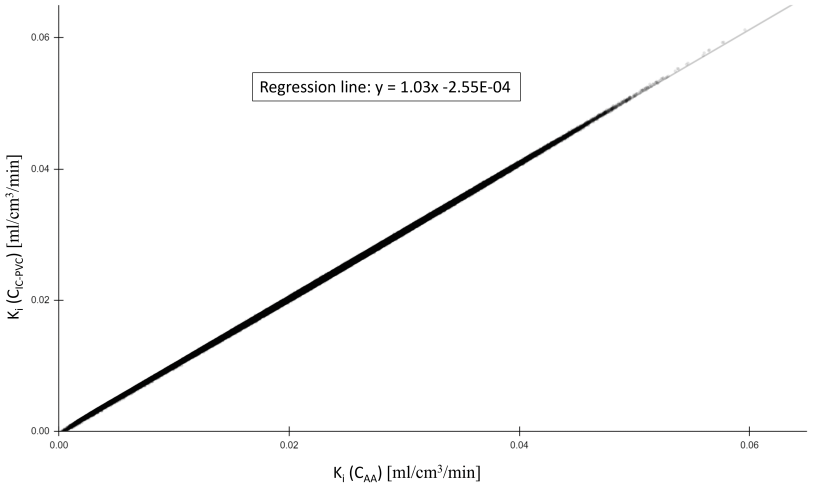

Figure 7: Regression analysis of the voxel-wise net influx rates obtained by using $C_{IC\text{-}PVC}$ and C_{AA} as subsequent input functions. The graph in this figure is an example of the analysis for one patient. The horizontal axis represents the net influx rates estimated by taking C_{AA} as the input function and the vertical axis represents the net influx rates estimated by using $C_{IC\text{-}PVC}$ as the input function.

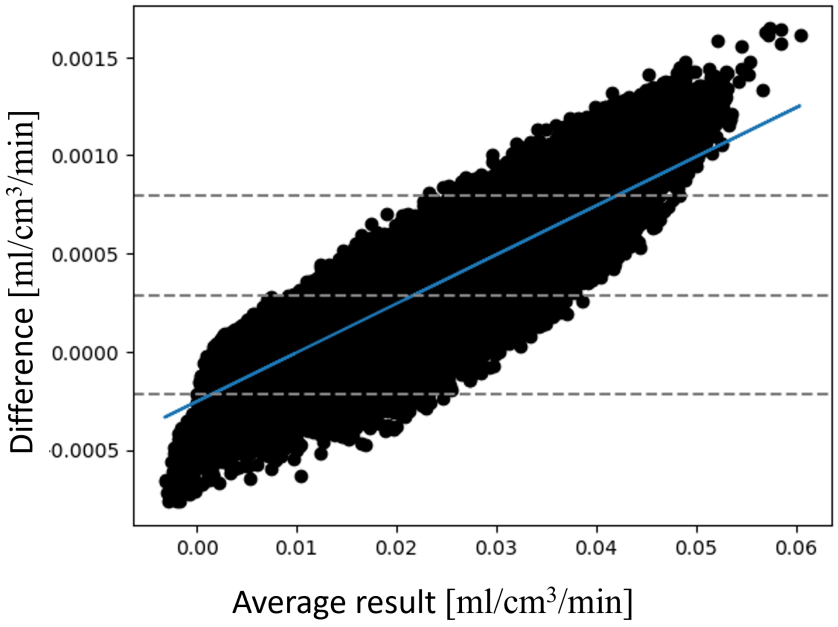

Figure 8: Bland-Altman plot of the voxel-wise net influx rate obtained by using $C_{IC\text{-}PVC}$ and C_{AA} as the input functions for the same patient as in Figure 7. The blue line is the regression line used to assess proportional bias in the estimates. The x-axis of Figure 8 represents the average result, i.e. the average of the net influx rates estimated by $C_{IC\text{-}PVC}$ and C_{AA}. The y-axis of the figure represents the difference between the net influx rate estimated by the two input functions, i.e. the net influx rate estimated by $C_{IC\text{-}PVC}$ minus the net influx rate estimated by C_{AA}. The three dashed lines represent, from top to bottom, the upper confidence interval, the mean difference, and the lower confidence interval, respectively.

Discussion

This study investigates the feasibility of using a carotids IDIF to estimate tracer kinetic rate constants in a non-invasive way, as an alternative to the commonly used arterial input function. The procedure used for this study is semi-automatic, to reduce the number of subjective steps and erroneous results. Manual determination was necessary to define the VOI containing the carotids and to select the appropriate blood-independent component image. The segmentation of the carotids and generation of the vessel and tissue mask was done automatically. The TACs obtained by applying the vessel and tissue mask to the dynamic brain FDG PET data were used for automatic PVE correction of the carotids TAC, by the use of the non-negative linear least squares method. The original and PVE-corrected TACs were then used for tracer kinetic modeling using a two-tissue compartment irreversible tracer model and Patlak analysis, and were compared to reference values obtained from kinetic modeling with an IDIF extracted from the ascending aorta.

An important assumption made for this this study is the assumption that the FDG concentration in blood plasma is equal to the FDG concentration in whole blood and therefore we can use the TAC of FDG in whole blood as the plasma input function. The validity of this assumption was established over a 120-minute period by a study previously done [Gambhir *et al.*, 1989]. Given that the scan duration in the current study was only 65 minutes, we can confidently make this assumption. If the procedure used in this study should be applied to a study where a different radioactive tracer is used, it may be necessary to correct the obtained whole-blood carotids TAC for radio-metabolite production and parent-to-whole-blood ratio. Although many studies have been conducted in recent years to propose methods to correct for metabolite concentration and parent fraction in plasma for different radioactive tracers [Harms *et al.*, 2016; He *et al.*, 2020; Sanabria-Bohórquez, 2003; Zanderigo *et al.*, 2018; Zanotti-Fregonara, Zoghbi, *et al.*, 2011], these methods need to be validated for all tracers and sometimes come with the drawback that this requires arterial blood samples.

The results in Figure 2 showed that the extraction of the blood-independent component image from the dynamic brain FDG PET data and the subsequent generation of the vessel and tissue masks was done successfully. The figure shows the contour of the carotids vessel mask in red and the contour of the tissue mask in blue. The threshold for creating the vessel mask was determined by the Gaussian fitting method and was set to 9 times the standard deviation. Using this method, a vessel mask of the common carotid arteries and parts of the internal and external carotid arteries was generated. The tissue mask was generated by dilating the previously created vessel mask using both a 3×3×3 and 5×5×5 structuring element and subsequent subtraction of one from the other. The use of structuring elements smaller than 3x3x3 resulted in a tissue mask that included parts of the carotid structures. Using a structuring element larger than 5x5x5 did not result in a significant difference in the obtained estimation.

In the results of this study, all three TACs, i.e. the original carotids TAC (C_{IC}), the PVE-corrected TAC of the carotids ($C_{IC\text{-}PVC}$), and the TAC extracted from the ascending aorta (C_{AA}), are shown to have a similar shape. Although it has been proposed that the input function can be estimated from the results of ICA directly [Naganawa *et al.*, 2005], the results in Figure 4 show that there is, on average, a large difference of 46% in peak height between C_{IC} and C_{AA}. To assess whether or not the C_{IC} could potentially be used as an alternative to the arterial input function, quantitative analysis was performed. The analysis showed that there was a good agreement between C_{IC} and C_{AA} in terms of the values estimated for the model parameter k_2, but significant differences for the model parameters K_1, k_3, K_i obtained by compartment modeling, and K_i obtained by Patlak analysis. This implies that the TAC that is estimated directly by ICA is not an appropriate alternative to use as an input function for quantitative brain FDG PET studies.

After partial volume correction, the obtained mean PVE-corrected TAC ($C_{IC\text{-}PVC}$) became more similar to C_{AA} and the peak of $C_{IC\text{-}PVC}$ was only 11% lower than the one of C_{AA}. The MPEs for all parameters except k_2 were significantly reduced. Moreover, performing a Wilcoxon signed-rank test revealed that the hypothesis of zero mean difference could not be rejected for the parameters K_1, k_3, K_i obtained by compartment modeling, and K_i obtained by Patlak analysis. Although it was shown that there is a significant difference between the model parameter k_2 estimated by $C_{IC\text{-}PVC}$ and C_{AA}, the mean value for k_2 (0.11 ± 0.03 min^{-1}) estimated by $C_{IC\text{-}PVC}$ is within the range of k_2 values that were previously published [Phelps *et al.*, 1979; Sari *et al.*, 2022]. Although there is a good agreement in terms of the obtained net influx rates, the errors in the parameters

K_1, k_2, and k_3 indicate that when employing $C_{IC\text{-}PVC}$, it is advisable to limit the outcome values to K_i, making it possible to limit kinetic modeling to only Patlak analysis.

Table 1 shows that the net influx rate estimated with C_{IC} as the input function for compartment modeling is, on average, an overestimate of the value for the net influx rate estimated with compartment modeling with C_{AA} as the input function. This is consistent with the findings from an earlier study by Naganawa *et al.* (2020) where they concluded that K_i was generally underestimated when the AUC of the input function was overestimated, and vice versa. From Figure 4 it was found that the AUC for the mean C_{IC}, $C_{IC\text{-}PVC}$, and C_{AA} were 450, 627, and 651 min.* kBq*cc^{-1}, respectively. This indicates that, on average, the AUC for C_{IC} is greatly underestimated, corresponding to an overestimate of the net influx rate. The AUC for $C_{IC\text{-}PVC}$ is only slightly smaller than the AUC of C_{AA}, which does not result in an overestimation of the net influx rate.

Estimation of model parameters using Patlak analysis uses the proportion of the input function for which the reversible compartment is in equilibrium with plasma, i.e. the frames of the last 35 minutes. As explained by Vriens *et al.* (2009), it can be deduced from the Patlak formula [Jodal, 2004] that an overestimation of the concentration of tracer in plasma leads to the underestimation of the net influx rate, and vice versa. In the later time frames, $C_{IC\text{-}PVC}$ and C_{AA} are almost equal (0.40% difference in the last frame) and C_{IC} is an underestimate of C_{AA} (17% difference in the last frame). The slight underestimation of $C_{IC\text{-}PVC}$ has shown to not affect the estimated net influx rate. The underestimation of the C_{IC} resulted in the overestimation of the net influx rate.

Since there are also patients for whom the PVE-corrected carotids TAC is an overestimate of the reference, according to Chen *et al.* (1998) it can be ruled out that dead-time is the error causing the underestimation. Studies previously conducted by Chen *et al.* (1998) and Zanotti-Fregonara, Fadaili, *et al.* (2009) have shown that the used temporal PET sampling may explain the discrepancy in the peak height of the IDIFs and that finer sampling is likely to improve the results. Furthermore, the difference in the obtained TACs can be explained by the fact that the IDIFs are extracted from different blood pools (i.e. the carotid arteries and the ascending aorta) with different dispersion effects [Feng *et al.*, 2019; Jochimsen *et al.*, 2016], which results in differences in the bolus dynamics [Oikonen, 2023]. For this study, the IDIFs were corrected for delay, but not for dispersion. For future research, it might be of interest to repeat the current study and include dispersion correction to assess how this affects the estimated model parameters. A possible method to correct for dispersion was previously proposed by Islam *et al.* (2017).

The results obtained with regression analysis of the regional net influx rates (Figure 6 and Table 2) support the previously reported observations of overestimation of the net influx rate by compartment modeling with C_{IC} compared to C_{AA}. Additionally, regression analysis to compare the net influx rates estimated by C_{IC} and C_{AA} using Patlak analysis showed a slope significantly larger than one and an intercept larger than zero, indicating a positive systemic and proportional bias in the values estimated with C_{IC} and C_{AA}. Regression analysis for the net influx rate estimated by $C_{IC\text{-}PVC}$ and C_{AA} by the use of Patlak analysis showed a regression slope close to one, an intercept close to zero, and a high coefficient of determination, indicating a good agreement between the methods.

Voxel-wise quantitative analysis by the use of parametric net influx rate images generated with $C_{IC\text{-}PVC}$ and C_{AA} as the input functions revealed interesting results. The results obtained through regression analysis of the voxel-wise net influx rate, i.e. the unit slope, zero intercept, and a high coefficient of determination, confirmed the findings that had been made with regional Patlak analysis. However, the whole-brain net influx rates obtained from the parametric images, i.e. the mean of the net influx rates of all voxels in the parametric images (Table 3), are lower than the regional, whole-brain net influx rates that were previously obtained by Patlak analysis (Table 1). A possible explanation for the underestimation of the net influx rate in parametric images is the fact that the voxel TACs that are used to generate the parametric images are very noisy [Kimura *et al.*, 1999]. The noisy nature of the TACs causes the inaccurate estimation of tracer concentration and the subsequent underestimation of the net influx rate. Another explanation for the underestimation might be the fact that the PVE, which is more pronounced in voxel-wise analysis than in regional analysis, can cause under- and overestimation of the tracer concentration in tissue [Aston *et al.*, 2002]. Finally, whereas regional analysis takes an average parameter value across all voxels in the VOI, voxel-wise analysis allows spatial heterogeneity in tissue to be assessed by looking at

each voxel separately. Since different areas within a VOI may exhibit variations in the underlying physiological processes, this can lead to different net influx rates, and hence different regional influx rates. Figure 8 shows the Bland-Altman plot corresponding to the results shown in Figure 7. To assess whether there is a systematic or proportional bias in the voxel-wise net influx rates estimated by the input functions $C_{\text{IC-PVC}}$ and C_{AA}, it was examined whether the mean differences and regression slopes observed for all patients were significantly different from zero. Although the trend and non-zero mean difference in the Bland-Altman plot in Figure 8 imply that there is a positive systemic and proportional bias in the estimation of the net influx rates for this patient, the Wilcoxon signed-rank test showed that there was neither a significant mean difference nor a significant slope for the voxel-wise net influx rates for the nine patients. This indicates that there is a neither systematic nor proportional bias between the voxel-wise net influx rates estimated by $C_{\text{IC-PVC}}$ and C_{AA}.

Although the entire procedure used for this study is non-invasive, it is important to keep in mind that this was made possible by using a PET scan with a large field-of-view that enabled the acquisition of dynamic whole-body FDG PET data. The dynamic FDG PET data of the heart region was used to extract an image-derived input function from the ascending aorta, which was then used for partial-volume correction. In conventional PET scanners, the field-of-view is narrower so this data of the heart region is not available. In case dynamic FDG PET data of this region is not available, a plasma input function at a minimum of three time-points will have to be measured by arterial blood sampling or another (non-invasive) alternative.

Conclusion

The results of this study suggest that an image-derived input function obtained from automatic segmentation of the carotids by independent component analysis and corrected for the partial volume effect can accurately be used as an alternative for the commonly used arterial blood sampled input function for brain FDG PET Patlak analysis. Despite the accurate results for the net influx rate estimated by the two-tissue compartment irreversible tracer model, the differences between the model parameters K_1, k_2, and k_3 estimated with the $C_{\text{IC-PVC}}$ and the C_{AA} suggest that the PVE-corrected carotids image-derived input function cannot be used as an accurate alternative input function for compartment modeling.

References

Aston, J. A. D., Cunningham, V. J., Asselin, M.-C., Hammers, A., Evans, A. C., & Gunn, R. N. (2002). Positron Emission Tomography Partial Volume Correction: Estimation and Algorithms. *Journal of Cerebral Blood Flow & Metabolism*, *22*(8), 1019–1034. https://doi.org/10.1097/00004647-200208000-00014

Bell, D., & Deng, F. (2019). F-18 fluorodeoxyglucose. https://doi.org/10.53347/rid-73056

Bettinardi, V., Castiglioni, I., Bernardi, E. D., & Gilardi, M. C. (2014). PET quantification: Strategies for partial volume correction. *Clinical and Translational Imaging*, *2*(3), 199–218. https://doi.org/10.1007/s40336-014-0066-y

Cardoso, J.-F. (2003). Dependence, Correlation and Gaussianity in Independent Component Analysis. *J. Mach. Learn. Res.*, *4*(null), 1177–1203.

Charlick, M., & Das, J. M. (2022). Anatomy, Head and Neck: Internal Carotid Arteries. *StatPearls*.

Chen, K., Bandy, D., Reiman, E., Huang, S.-C., Lawson, M., Feng, D., Yun, L.-s., & Palant, A. (1998). Noninvasive Quantification of the Cerebral Metabolic Rate for Glucose Using Positron Emission Tomography, ^{18}F-Fluoro-2-Deoxyglucose, the Patlak Method, and an Image-Derived Input Function. *Journal of Cerebral Blood Flow & Metabolism*, *18*(7), 716–723. https://doi.org/10.1097/00004647-199807000-00002

Dieckmann, J. (2023). Introduction to ICA: Independent Component Analysis. *Medium*.

Feng, T., Zhao, Y., Shi, H., Li, H., Zhang, X., Wang, G., Badawi, R. D., Price, P. M., Jones, T., & Cherry, S. R. (2019). The Effects of Delay on the Input Function for Early Dynamics in Total Body Parametric Imaging. *2019 IEEE Nuclear Science Symposium and Medical Imaging Conference (NSS/MIC)*. https://doi.org/10.1109/nss/mic42101.2019.9059886

Gambhir, S., Schwaiger, M., Huang, S., Krivokapich, J., Schelbert, H., Nienaber, C., & Phelps, M. (1989). Simple noninvasive quantification method for measuring myocardial glucose utilization in humans employing positron emission tomography and fluorine-18 deoxyglucose. *Journal of nuclear medicine : official publication, Society of Nuclear Medicine*, *30*, 359–66.

Grinstead, C. M., & Snell, J. L. (2022). 9.1: Central Limit Theorem for Bernoulli Trials. *Libretexts*.

Harms, H. J., Huisman, M. C., Rijnierse, M. T., Greuter, H., Hsieh, Y.-L., de Haan, S., Schuit, R. C., Knaapen, P., Lubberink, M., & Lammertsma, A. A. (2016). Noninvasive Quantification of Myocardial ^{11}C-Meta-Hydroxyephedrine Kinetics. *Journal of Nuclear Medicine*, *57*(9), 1376–1381. https://doi.org/10.2967/jnumed.115.167437

He, X., Wedekind, F., Kroll, T., Oskamp, A., Beer, S., Drzezga, A., Ermert, J., Neumaier, B., Bauer, A., & Elmenhorst, D. (2020). Image-Derived Input Functions for Quantification of A_1 Adenosine Receptors Availability in Mice Brains Using PET and [^{18}F]CPFPX. *Frontiers in Physiology*, *10*. https://doi.org/10.3389/fphys.2019.01617

Heurling, K., Leuzy, A., Jonasson, M., Frick, A., Zimmer, E. R., Nordberg, A., & Lubberink, M. (2017). Quantitative positron emission tomography in brain research. *Brain Research*, *1670*, 220–234. https://doi.org/https://doi.org/10.1016/j.brainres.2017.06.022

Huang, S. C., Phelps, M. E., Hoffman, E. J., Sideris, K., Selin, C. J., & Kuhl, D. E. (1980). Noninvasive determination of local cerebral metabolic rate of glucose in man. *American Journal of Physiology-Endocrinology and Metabolism*, *238*(1), E69–E82. https://doi.org/10.1152/ajpendo.1980.238.1.e69

Hyvarinen, A. (1999). Fast and robust fixed-point algorithms for independent component analysis. *IEEE Transactions on Neural Networks*, *10*(3), 626–634. https://doi.org/10.1109/72.761722

Hyvärinen, A., & Oja, E. (2000). Independent component analysis: Algorithms and applications. *Neural Networks*, *13*(4-5), 411–430. https://doi.org/10.1016/s0893-6080(00)00026-5

Islam, M. M., Tsujikawa, T., Mori, T., Kiyono, Y., & Okazawa, H. (2017). Estimation of arterial input by a noninvasive image derived method in brain $H_2{}^{15}O$ PET study: Confirmation of arterial location using MR angiography. *Physics in Medicine and Biology*, *62*(11), 4514–4524. https://doi.org/10.1088/1361-6560/aa6a95

Jochimsen, T. H., Zeisig, V., Schulz, J., Werner, P., Patt, M., Patt, J., Dreyer, A. Y., Boltze, J., Barthel, H., Sabri, O., & Sattler, B. (2016). Fully automated calculation of image-derived input function in simultaneous PET/MRI in a sheep model. *EJNMMI Physics*, *3*(1). https://doi.org/10.1186/s40658-016-0139-2

Jodal, L. (2004). Interpretation of Patlak plot.

Kilicoglu, O., Sepay, N., Ozgenc, E., Gundogdu, E., Kara, U., Alomairy, S., & Al-Buriahi, M. (2023). Evaluation of F-18 FDG radiopharmaceuticals through Molecular Docking and radiation effects. *Applied Radiation and Isotopes*, *191*, 110553. https://doi.org/10.1016/j.apradiso.2022.110553

Kimura, Y., Hsu, H., Toyama, H., Senda, M., & Alpert, N. M. (1999). Improved Signal-to-Noise Ratio in Parametric Images by Cluster Analysis. *NeuroImage*, *9*(5), 554–561. https://doi.org/10.1006/nimg.1999.0430

Krejza, J., Arkuszewski, M., Kasner, S. E., Weigele, J., Ustymowicz, A., Hurst, R. W., Cucchiara, B. L., & Messe, S. R. (2006). Carotid Artery Diameter in Men and Women and the Relation to Body and Neck Size. *Stroke*, *37*(4), 1103–1105. https://doi.org/10.1161/01.str.0000206440.48756.f7

Kumar, M., & Jayanthi, V. E. (2019). Blind source separation using kurtosis, negentropy and maximum likelihood functions. *International Journal of Speech Technology*, *23*(1), 13–21. https://doi.org/10.1007/s10772-019-09664-z

Meikle, S. R., Sossi, V., Roncali, E., Cherry, S. R., Banati, R., Mankoff, D., Jones, T., James, M., Sutcliffe, J., Ouyang, J., Petibon, Y., Ma, C., Fakhri, G. E., Surti, S., Karp, J. S., Badawi, R. D., Yamaya, T., Akamatsu, G., Schramm, G., … Dutta, J. (2021). Quantitative PET in the 2020s: A roadmap. *Physics in Medicine & Biology*, *66*(6), 06RM01. https://doi.org/10.1088/1361-6560/abd4f7

Mejia, M. A., Itoh, M., Watabe, H., Fujiwara, T., & Nakamura, T. (1994). Simplified Nonlinearity Correction of Oxygen-15-Water Regional Cerebral Blood Flow Images without Blood Sampling. *Journal of Nuclear Medicine*, *35*(11), 1870–1877. https://jnm.snmjournals.org/content/35/11/1870

Naganawa, M., Kimura, Y., Ishii, K., Oda, K., Ishiwata, K., & Matani, A. (2005). Extraction of a plasma time-activity curve from dynamic brain PET images based on independent component analysis. *IEEE Transactions on Biomedical Engineering*, *52*(2), 201–210. https://doi.org/10.1109/TBME.2004.840193

Naganawa, M., Gallezot, J.-D., Shah, V., Mulnix, T., Young, C., Dias, M., Chen, M.-K., Smith, A. M., & Carson, R. E. (2020). Assessment of population-based input functions for Patlak imaging of whole body dynamic ^{18}F-FDG PET. *EJNMMI Physics*, *7*(1). https://doi.org/10.1186/s40658-020-00330-x

Oikonen, V. (2023). Dispersion of input function. http://www.turkupetcentre.net/petanalysis/input_dispersion.html

Phelps, M. E., Huang, S. C., Hoffman, E. J., Selin, C., Sokoloff, L., & Kuhl, D. E. (1979). Tomographic measurement of local cerebral glucose metabolic rate in humans with (F-18)2-fluoro-2-deoxy-D-glucose: Validation of method. *Annals of Neurology*, *6*(5), 371–388. https://doi.org/https://doi.org/10.1002/ana.410060502

Rahmim, A., Lodge, M. A., Karakatsanis, N. A., Panin, V. Y., Zhou, Y., McMillan, A., Cho, S., Zaidi, H., Casey, M. E., & Wahl, R. L. (2018). Dynamic whole-body PET imaging: principles, potentials and applications. *European Journal of Nuclear Medicine and Molecular Imaging*, *46*(2), 501–518. https://doi.org/10.1007/s00259-018-4153-6

Sanabria-Bohórquez, S. (2003). Image-Derived Input Function for [^{11}C]Flumazenil Kinetic Analysis in Human Brain. *Molecular Imaging & Biology*, *5*(2), 72–78. https://doi.org/10.1016/s1536-1632(03)00046-5

Sari, H., Mingels, C., Alberts, I., Hu, J., Buesser, D., Shah, V., Schepers, R., Caluori, P., Panin, V., Conti, M., Afshar-Oromieh, A., Shi, K., Eriksson, L., Rominger, A., & Cumming, P. (2022). First results on kinetic modelling and parametric imaging of dynamic ^{18}F-FDG datasets from a long axial FOV PET scanner in oncological patients. *European Journal of Nuclear Medicine and Molecular Imaging*, *49*(6), 1997–2009. https://doi.org/10.1007/s00259-021-05623-6

Schmidt, K., Lucignani, G., Moresco, R. M., Rizzo, G., Gilardi, M. C., Messa, C., Colombo, F., Fazio, F., & Sokoloff, L. (1992). Errors Introduced by Tissue Heterogeneity in Estimation of Local Cerebral Glucose Utilization with Current Kinetic Models of the [^{18}F]Fluorodeoxyglucose Method. *Journal of Cerebral Blood Flow & Metabolism*, *12*(5), 823–834. https://doi.org/10.1038/jcbfm.1992.114

Su, K.-H., Wu, L.-C., Liu, R.-S., Wang, S.-J., & Chen, J.-C. (2005). Quantification method in [^{18}F]fluorodeoxyglucose brain positron emission tomography using independent component

analysis. *Nuclear Medicine Communications*, *26*(11), 995–1004. https://doi.org/10.1097/01.mnm.0000184999.81203.5c

Tai, Y. F., & Piccini, P. (2004). Applications of positron emission tomography (PET) in neurology. *Journal of Neurology, Neurosurgery & Psychiatry*, *75*(5), 669–676. https://doi.org/10.1136/jnnp.2003.028175

Tharwat, A. (2020). Independent component analysis: An introduction. *Applied Computing and Informatics*, *17*(2), 222–249. https://doi.org/10.1016/j.aci.2018.08.006

Thie, J. A. (2004). Understanding the Standardized Uptake Value, Its Methods, and Implications for Usage. *Journal of Nuclear Medicine*, *45*(9), 1431–1434. https://jnm.snmjournals.org/content/45/9/1431

Vallabhajosula, S. (2023). Pharmacokinetics and Modeling. In *Molecular imaging and targeted therapy* (pp. 291–302). Springer International Publishing. https://doi.org/10.1007/978-3-031-23205-3_13

van der Weijden, C. W. J., Mossel, P., Bartels, A. L., Dierckx, R. A. J. O., Luurtsema, G., Lammertsma, A. A., Willemsen, A. T. M., & de Vries, E. F. J. (2023). Non-invasive kinetic modelling approaches for quantitative analysis of brain PET studies. *European Journal of Nuclear Medicine and Molecular Imaging*, *50*(6), 1636–1650. https://doi.org/10.1007/s00259-022-06057-4

van Sluis, J., van Snick, J. H., Brouwers, A. H., Noordzij, W., Dierckx, R. A. J. O., Borra, R. J. H., Lammertsma, A. A., Glaudemans, A. W. J. M., Slart, R. H. J. A., Yaqub, M., Tsoumpas, C., & Boellaard, R. (2022). Shortened duration whole body ^{18}F-FDG PET Patlak imaging on the Biograph Vision Quadra PET/CT using a population-averaged input function. *EJNMMI Phys.*, *9*(1). https://doi.org/10.1186/s40658-022-00504-9

Vriens, D., de Geus-Oei, L.-F., Oyen, W. J., & Visser, E. P. (2009). A Curve-Fitting Approach to Estimate the Arterial Plasma Input Function for the Assessment of Glucose Metabolic Rate and Response to Treatment. *Journal of Nuclear Medicine*, *50*(12), 1933–1939. https://doi.org/10.2967/jnumed.109.065243

Wang, K. (2018). Feasibility of High Spatial Resolution Working Modes for Clinical PET Scanner. *International Journal of Medical Physics, Clinical Engineering and Radiation Oncology*, *07*(04), 539–552. https://doi.org/10.4236/ijmpcero.2018.74045

Watabe, H., Ikoma, Y., Kimura, Y., Naganawa, M., & Shidahara, M. (2006). PET kinetic analysis—compartmental model. *Annals of Nuclear Medicine*, *20*(9), 583–588. https://doi.org/10.1007/bf02984655

Weber, W. A. (2010). Quantitative analysis of PET studies [PET in Radiotherapy Planning]. *Radiotherapy and Oncology*, *96*(3), 308–310. https://doi.org/https://doi.org/10.1016/j.radonc.2010.07.004

Zanderigo, F., Kang, Y., Kumar, D., Nikolopoulou, A., Mozley, P. D., Kothari, P. J., He, B., Schlyer, D., Rapoport, S. I., Oquendo, M. A., Vallabhajosula, S., Mann, J. J., & Sublette, M. E. (2018). [^{11}C]arachidonic acid incorporation measurement in human brain: Optimization for clinical use. *Synapse*, *72*(2), e22018. https://doi.org/10.1002/syn.22018

Zanotti-Fregonara, P., Chen, K., Liow, J.-S., Fujita, M., & Innis, R. B. (2011). Image-Derived Input Function for Brain PET Studies: Many Challenges and Few Opportunities. *Journal of Cerebral Blood Flow & Metabolism*, *31*(10), 1986–1998. https://doi.org/10.1038/jcbfm.2011.107

Zanotti-Fregonara, P., Fadaili, E. M., Maroy, R., Comtat, C., Souloumiac, A., Jan, S., Ribeiro, M.-J., Gaura, V., Bar-Hen, A., & Trébossen, R. (2009). Comparison of Eight Methods for the Estimation of the Image-Derived Input Function in Dynamic [^{18}F]-FDG PET Human Brain Studies. *Journal of Cerebral Blood Flow & Metabolism*, *29*(11), 1825–1835. https://doi.org/10.1038/jcbfm.2009.93

Zanotti-Fregonara, P., Maroy, R., Comtat, C., Jan, S., Gaura, V., Bar-Hen, A., Ribeiro, M.-J., & Trébossen, R. (2009). Comparison of 3 Methods of Automated Internal Carotid Segmentation in Human Brain PET Studies: Application to the Estimation of Arterial Input Function. *Journal of Nuclear Medicine*, *50*(3), 461–467. https://doi.org/10.2967/jnumed.108.059642

Zanotti-Fregonara, P., Zoghbi, S. S., Liow, J.-S., Luong, E., Boellaard, R., Gladding, R. L., Pike, V. W., Innis, R. B., & Fujita, M. (2011). Kinetic analysis in human brain of [^{11}C](R)-rolipram, a positron emission tomographic radioligand to image phosphodiesterase 4: A retest study and use of an image-derived input function. *NeuroImage*, *54*(3), 1903–1909. https://doi.org/10.1016/j.neuroimage.2010.10.064